

Structure and properties of oxygen centers in CaF₂ crystals from *ab initio* embedded cluster calculations

Andrey S. Mysovsky,^{1,*} Peter V. Sushko,^{2,3} Evgeny A. Radzhabov,¹ Michael Reichling,⁴ and Alexander L. Shluger^{2,3}

¹*Vinogradov Institute of Geochemistry, Russian Academy of Science, Siberian Branch, 1a Favorsky St., 664033 Irkutsk, Russia*

²*Department of Physics and Astronomy and London Centre for Nanotechnology, University College London, Gower Street, London WC1E 6BT, United Kingdom*

³*WPI-Advanced Institute for Materials Research, Tohoku University, Sendai 980-8577, Japan*

⁴*Fachbereich Physik, Universität Osnabrück, Barbarastrasse 7, 49076 Osnabrück, Germany*

(Received 6 February 2011; revised manuscript received 26 July 2011; published 31 August 2011)

We present the results of *ab initio* calculations of several intrinsic and oxygen-containing defects in CaF₂ including an *F* center, a substitutional O⁻ ion, an O²⁻-vacancy dipole, and *F_A*(O²⁻) and *F_{2A}*⁺(O²⁻) centers. The calculations have been performed using a hybrid density functional and an embedded cluster method. The calculated optical absorption (OA) spectra and magnetic properties are in a very good agreement with available experimental data. It is suggested that isolated substitutional O⁻ ions induce an OA band in the vacuum ultraviolet region at about 7 eV. The nature of the OA bands associated with O²⁻-vacancy dipoles and other, more complex, defects is clarified and corresponding luminescence mechanisms are discussed.

DOI: [10.1103/PhysRevB.84.064133](https://doi.org/10.1103/PhysRevB.84.064133)

PACS number(s): 61.72.Bb, 71.15.Mb, 61.72.J-, 66.30.hd

I. INTRODUCTION

Calcium fluoride is a suitable material for a variety of laser optical applications in the ultraviolet spectral region. It can, for instance, be used for generating high-order harmonics¹ and white light²⁻⁵ from ultrashort laser pulses. Due to its very large band gap (12.1 eV),⁶ CaF₂ is one of few materials suitable for lenses and optical windows in lithography systems operating in the deep ultraviolet (DUV) and vacuum ultraviolet (VUV) spectral regions⁷⁻⁹ with, potentially, significant economic impact.

It is now possible to produce large-size CaF₂ single crystals of highest purity.¹⁰⁻¹² However, there remain issues limiting the use of CaF₂ for highly demanding ultraviolet (UV) applications. In particular, intrinsic birefringence,¹³⁻¹⁵ and even trace concentrations of defects, can be detrimental to the material's optical properties.¹⁶ For example, rare-earth impurities¹⁷ and oxygen defects^{18,19} may induce unwanted laser beam distortion, optical absorption,²⁰ and promote material damage.^{21,22}

One of the main obstacles to exploiting the full potential of CaF₂ is the presence of oxygen centers, having an optical absorption in the ultraviolet region.²³⁻²⁶ Therefore, we undertook a comprehensive effort for calculating geometrical structures and optical properties of oxygen centers and related defects in CaF₂. As several of these defects may be detected and identified using electron paramagnetic resonance (EPR) spectroscopy, we complement our studies by calculating the hyperfine (*hf*) coupling constants, where appropriate.

In "as-grown" CaF₂ crystals, substitutional oxide ion impurities are compensated by anion vacancies (*V_A*) and form O²⁻-*V_A* complexes.^{27,28} Since the formal charges of a substitutional O²⁻ and an anion vacancy with respect to their lattice sites are -1 and +1, respectively, these complexes are often called O²⁻-*V_A* dipoles. Three optical absorption (OA) bands, all in the VUV region, are assigned to this defect. Characteristics of the bands peaking at 6.7 and 8.4 eV are firmly established,^{29,30} while exact position and the width of the third, higher energy, band are still debated. Authors of

Ref. 30 suggest that the maximum of this band is at 9.2 eV, while, according to Ref. 29, it is at 9.8 eV. We note that high-precision measurements of the optical absorption at the energies above 9 eV are complicated due to proximity to the bulk exciton absorption at about 10 eV. Excitation in all three bands of O²⁻-*V_A* dipoles leads to the same luminescence band with the maximum at 2.6 eV and a spectral width of 0.5 eV.

Excitation in the second and third bands can result in photodissociation of the O²⁻-*V_A* dipoles if the temperature exceeds 200 K.²³ The same effect can be achieved by x-ray irradiation of the crystal and by its exposure to UV light with energy higher than the excitonic absorption edge. As a result of the photodissociation, the concentration of the O²⁻-*V_A* dipoles decreases and other defect species, such as isolated substitutional O⁻ ions and complexes of O²⁻ with neutral and charged anion vacancies [*F_A*(O²⁻) and *F_{2A}*⁺(O²⁻) centers], are observed.²³

While the main stages of the photodissociation mechanism have been clarified earlier,³¹ other processes taking place in oxygen-containing CaF₂ crystals are much less understood. In particular, thermoactivated transformation of the photodissociation products, i.e. O⁻ ions, *F_A*(O²⁻) and *F_{2A}*⁺(O²⁻) centers, observed at room temperature and above, leads to a partial replenishment of the O²⁻-*V_A* dipoles. The nature of this transformation is yet unknown.

On the theory front, modeling of anion vacancies³²⁻³⁸ and their complexes with oxygen impurities^{39,40} face several challenges.

First, electronic centers such as a neutral anion vacancy, i.e., an *F* center, can have complex long-range charge density distributions. For example, the hyperfine interaction of the *F* center with the lattice F atoms is known to extend to the seventh shell of the anions around the vacancy site.⁴¹⁻⁴³ Therefore, accurate modeling of the magnetic properties of these defects requires describing a large number of atoms near them quantum mechanically.

Second, oxygen defects in CaF₂ have absorption energies in the deep UV region, which can only be described theoretically

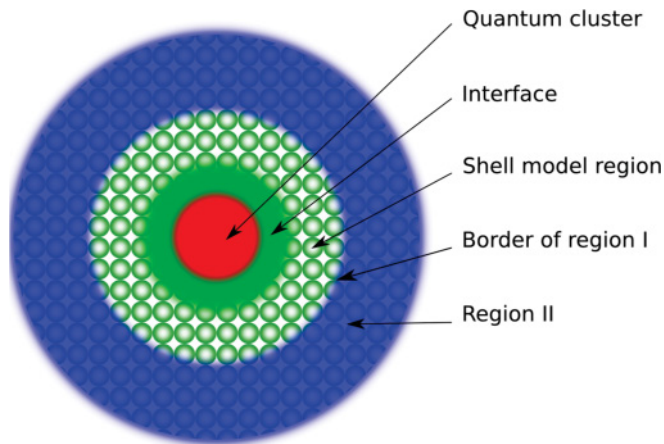


FIG. 1. (Color online) Schematic setup for the embedded cluster calculations. See the main text for the sizes of each region.

if the material's band gap is reproduced well. This, in turn, requires using *ab initio* methods more accurate than the standard DFT methods based on the local density and generalized gradient approximations.³⁷

Finally, vacancies and substitutional oxygen impurities aggregate into complex defects, such as $O^{2-}-V_A$ and $F_{2A}^+(O^{2-})$ centers, which form convoluted patterns of defect-induced atomic displacements. These displacements involve several tens of atoms near the defect site, yet, they need to be taken into account as they affect defect spectroscopic characteristics, in particular, the values of the hyperfine coupling constants and luminescence energies.

The purpose of this paper is to make an accurate calculation of complex defects in the bulk CaF_2 and to predict their spectroscopic properties. Detailed quantitative understanding of the spectroscopic properties of these defects is crucial for developing predictive models of defect-induced processes in this materials.

II. CALCULATION DETAILS

We employed a hybrid embedded cluster method in which a cluster, formed by a defect and its nearest surrounding, is considered quantum mechanically (QM cluster) and is embedded into the remaining part of the system, which is represented classically. In this approach, an infinite crystal is modeled using a large finite cluster containing several thousand atoms and called *nanocluster*. The nanocluster is divided into regions I and II, as shown in Fig. 1. Region I includes several hundred atoms and is divided into (i) a QM cluster with a defect and surrounding atoms treated using an *ab initio* technique, (ii) an interface region, connecting the quantum cluster to the rest of the solid, and (iii) the remainder of region I modeled using the classical shell model.

Atoms of the interface region have a dual nature and interact quantum mechanically with the QM cluster and classically with the rest of the nanocluster. Region I is surrounded by a finite region II, which is treated atomistically. The classical ions in regions I and II are treated using the shell model⁴⁴ and interact with each other via interatomic potentials. Both quantum and classical atoms in region I are allowed to move in the course of the calculations. Positions of the QM atoms and

classical cores and shells are determined simultaneously using an effective energy minimization scheme. Atoms in region II are kept fixed in their ideal, bulk positions and provide correct potential energy surface for the atoms inside region I. The QM contributions to the total energy and forces are calculated using the Gaussian package for *ab initio* calculations of atoms and molecules.⁴⁵ This embedded cluster method is implemented in a computer code GUESS and its application to ionic and polar materials, molecular crystals, and metal-organics interfaces is described in details elsewhere.⁴⁶⁻⁵¹

A. Nanocluster, regions I and II, and the QM clusters

The nanocluster is constructed so the site-to-site variations of the electrostatic potential in its inner region reproduce well the electrostatic potential variations in the bulk CaF_2 . To achieve this, we selected a cubic lattice building block $Ca^{2+}(\frac{1}{4}F^-)_8$, in which the Ca^{2+} ion is located at the cube center and eight fractions of the fluorine ion ($\frac{1}{4}F^-$) are located at the cube corners. Each such building block is neutral and has no dipole moment. Then, a spherical nanocluster of ~ 32 Å radius is assembled from these building blocks. By construction, the nanocluster is neutral and has no dipole moment.

It is important to note that, while the site-to-site variations of the electrostatic potential inside the nanocluster are the same as in the CaF_2 bulk, in general, the absolute values of the potential differ. This is because not all components of the Cartesian quadrupole moments of the $Ca^{2+}(\frac{1}{4}F^-)_8$ building blocks are equal to zero and, as discussed in Ref. 52, the potential inside the nanocluster is determined by its shape. This has no effect on the calculated values of the physical properties discussed in this paper. A general method of eliminating an arbitrary number of the electric multipole moments in any crystal cell in order to provide the absolute convergence of the lattice electric potential is discussed elsewhere.^{52,53}

The shape and size of region I are defined by the problem at hand and should allow one to account for the defect-induced lattice relaxation accurately. In all calculations reported in this paper, we use a spherical region I, which is located at the center of the nanocluster, has the radius of ~ 13 Å, and contains about 700 ions. This is sufficient to account for most of the defect-induced lattice relaxation. The remaining part of the nanocluster (region II) is sufficiently large to provide an accurate potential energy surface for the atoms inside region I.

The QM cluster is located at the center of region I. Since the charges associated with F^- and Ca^{2+} ions deviate from their formal values, significant deviation of a QM cluster stoichiometry (Ca_mF_n) from that of the crystal (Ca_kF_{2k}) can lead to the cluster being overcharged either negatively or positively. However, fully stoichiometric clusters often have low symmetry and low compactness. Thus, for each considered defect, the size and shape of the QM clusters is selected in order to make them simultaneously as stoichiometric, compact, and symmetric, as possible.

The following QM clusters were selected according to this rule and used to model the point defects in the present work: Ca_4F_7 and $Ca_{16}F_{33}$ for the F center and substitutional O^- ion, $Ca_{14}F_{28}$ for the $O^{2-}-V_A$ dipole and the $F_A(O^{2-})$ center and $Ca_{18}F_{40}$ for the $F_{2A}^+(O^{2-})$ center.

TABLE I. Parameters of the shell model and interatomic potentials. The interface correction applies to the pairs of Ca atoms of the interface region and F atoms of the QM cluster only. A, ρ, C are parameters of the Buckingham potential $U(r) = A \exp(-r/\rho) - C/r^6$. Y is the shell charge, k is the spring constant. Elastic constants C_{11} , C_{12} , and C_{44} are given in GPa. Total charges of Ca and F ions are +2 and -1, respectively.

	A (eV)	ρ (Å)	C (eV Å ⁶)		
Classical region					
Ca-F	1326.32	0.3001	0.10		
F-F	1323.19	0.2687	17.81		
Interface correction					
Ca-F	500.00	0.3001	0.10		
Shell parameters					
F	Y ($ e $)		k (eV Å ²)		
	-2.38		67.02		
Elastic and dielectric constants					
	ϵ_0	ϵ_∞	C_{11}	C_{12}	C_{44}
This paper	6.38	1.87	158.9	42.1	21.2
Experiment (Ref. 56)	6.76	2.06	164.0	53.0	33.7

It is well known⁵⁴ that the crystalline environment, represented using the shell model, can artificially perturb the charge density distribution within the QM cluster due to the electrostatic interaction of electron density and the positive charges associated with the shell-model ions. To avoid this, we introduce an interface region (see Fig. 1) in which cations situated within 7 Å from any of the QM cluster ions are modeled using LANL1 effective core pseudopotentials (ECPs).⁵⁵ There are no basis functions associated with the interface cations.

B. Classical interatomic potentials

In this paper, we used the shell-model parameters reported in Ref. 57 and slightly adjusted them in order to provide consistency between the quantum-mechanical and the shell-model regions. Parameters of the Buckingham-type two-body potentials were fitted to the lattice constant of 5.52 Å, which is slightly larger than the experimental value of 5.462 Å, but more consistent with the optimized geometrical structures of the QM clusters. The obtained parameters are shown in Table I together with the dielectric and elastic constants of CaF₂ crystal calculated with this parameter set and those obtained experimentally.

Since a part of the non-Coulombic short-range interaction of the interface Ca ions with the atoms of the QM cluster is taken into account quantum mechanically, only a corrective interaction between the interface Ca ions and the fluorine ions in the QM cluster is needed. This is fitted in order to minimize the local structure distortion at the interface. The corresponding parameters are also shown in Table I.

C. Choice of quantum-mechanical method and basis set

Accounting accurately for the electronic correlation is crucial for the correct description of localized electronic states of defects. It is known that the Hartree-Fock (HF) method and density functional theory (DFT) within the generalized

gradient approximation (GGA) can give not only quantitatively inaccurate, but also qualitatively incorrect, defect electronic structures.^{58–60} For example, the HF calculation of a V_K center in the CaF₂ crystal predicts that the electronic hole is localized on one of the lattice fluorine ions. This is qualitatively different from a firmly established electronic structure of the V_K center, in which the hole is localized on two neighboring fluorines forming an F_2^- molecular ion.⁶¹

We used a hybrid density functional based on the three-parameter exchange-correlation functional B3LYP,^{62,63} which was modified so as to increase the relative weight of the HF exchange contribution from 20% to 40%. This hybrid functional is further referred to as B3LYP-40. Such a modification of the B3LYP exchange part has been used, and discussed in details, previously in, for example, Refs. 58, 59, and 64. For the purpose of this work, we found that B3LYP-40 provides accurate descriptions of both electronic and hole centers, i.e., the F center, which has an electron state in the band gap, and the V_K center,⁶¹ which has a hole state in the band gap. Hence, it is sufficiently robust to be used for a wide range of defects in the bulk CaF₂.

Optical transition energies were calculated using the time-dependent DFT (TDDFT) method.⁶⁵ Where it was possible, we applied also the Δ SCF method, in which the optical transition energies are calculated as the difference between the total energies of the excited and ground states, both of which are calculated with the same self-consistent field (SCF) method. This method is straightforward to apply if (i) the ground state and the excited state of interest have different multiplicities, e.g., they are singlet and triplet spin states, respectively; and (ii) the ground and the excited states have different symmetries, i.e., they belong to different irreducible representations of the symmetry group of the defect.

The choice of the basis set is also of crucial importance for predicting the correct electronic structure of the defects. In particular, since the lattice anions and the electron-containing anion vacancies have different spatial distributions of the electron density, atomic Gaussian-type basis sets may provide poor description of such electron-containing anion vacancies.

Therefore, in order to select the optimal basis set for the defects considered in this work, we have investigated the dependence of the F center hf constants, which provide a direct measure of the defect spin density distribution in the F center, on the quality of the basis sets and compared the obtained results to the experimental data.⁴¹ The calculations were performed using the smallest cluster Ca₄F₇ and did not include geometry relaxation near the F center in order to reduce the computational cost. Neglecting the lattice deformation in this case is justified since, according to the literature^{31,32} and our calculations reported below, this deformation is very small.

In order to optimize the basis set, we have considered the effect of the number, radius, and orbital momentum of the basis functions located at the vacancy site, and on the anions and cations neighboring to the vacancy.

Comparison of the calculated hf constants and the experimental data suggests that (i) basis set on the vacancy consisting of sp and f shells dramatically improves the agreement between calculated and experimental characteristics, (ii) further improvement is achieved by using polarization d shells on the cations, and (iii) d shells on the anions have almost no effect

TABLE II. Calculated and experimentally observed values of the hyperfine coupling constants (in Gauss) for the fluorine ions near the F center.

Ion	Axis	1				2				3				4			
		Ca ₄ F ₇				Ca ₁₆ F ₃₃				Ca ₁₆ F ₃₃				Expt. (Ref. 41)			
		BASIS1				BASIS1				LANL2DZ							
F(100)	A ₁	(100)	89.29	88.15	113.25	79.07											
	A ₂	(011)	59.45	64.65	86.73	58.95											
	A ₃	(01 $\bar{1}$)	59.34	64.20	86.59	57.38											
F(110)	A ₁	(110)		6.24	9.90	5.14											
	A ₂	(001)		4.29	7.10	3.27											
	A ₃	(1 $\bar{1}$ 0)		4.25	7.09	3.18											
F(111)	A ₁	(111)		9.63	4.09	9.75											
	A ₂ = A ₃	\perp		5.90	2.12	6.54											
F(11 $\bar{1}$)	A ₁	(11 $\bar{1}$)		3.10	3.40	1.97											
	A ₂ = A ₃	\perp		1.69	2.28	1.01											
F(200)	A ₁	(100)		2.04	2.56	1.68											
	A ₂ = A ₃	\perp		1.13	1.49	0.90											

on the calculated characteristics. On the basis of this analysis, we have selected the basis set for all subsequent calculations, unless explicitly stated otherwise, and denoted it as BASIS1.

BASIS1 includes (i) one s , one sp , and one f shell on the anion vacancy site with the orbital exponents of 0.1, 0.05, and 0.064 Bohr⁻², respectively; (ii) standard Pople's 6-31G basis on all anions, i.e., fluorine and oxygen; (iii) 6-31G basis with two additional polarization d shells from 6-311G* on calcium ions located near the defect; (iv) LANL2DZ without the most diffuse p shell and the corresponding LANL2 ECP for all other cations of the QM cluster. The latter modification of the LANL2DZ basis set does not significantly affect the accuracy of the calculations, yet, it reduces the cost of the computations for large QM clusters. With this basis set, the calculated hf constants ($A_1 = 89.29$ G, $A_2 = 59.45$ G, $A_3 = 59.34$ G) are very close to the corresponding values obtained experimentally ($A_1 = 79.07$ G, $A_2 = 58.95$ G, $A_3 = 57.38$ G).⁴²

III. RESULTS AND DISCUSSION

First, we investigate properties of isolated F center, anion vacancy, and substitutional oxygen ion impurities and then consider complexes of these defects.

A. F center

F centers in CaF₂ have been experimentally characterized in great details as early as in the 1960s.⁴¹⁻⁴³ Their optical absorption as well as hyperfine couplings up to the seventh shell of neighboring ions are known. However, there are no theoretical calculations of the F center approaching the same level of accuracy and detail.

One can better understand the difficulties accompanying theoretical modeling of the F center from Table II, where we compare the values of the F center hf constants obtained experimentally with those calculated using several QM clusters and basis sets. The experimental values are shown in the last column of the table. Positions and labels of nonequivalent fluorine neighbors to the F center are indicated in Fig. 2.

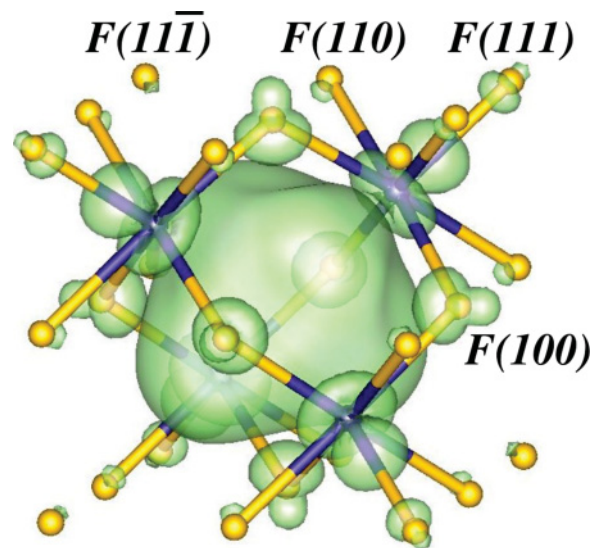


FIG. 2. (Color online) Surface of the constant spin density calculated for an isolated bulk F center. Dark (blue) and light (yellow) spheres are Ca and F atoms, respectively.

These values show a quite unusual peculiarity: the hf couplings for the F(111) ion, situated on the cube diagonal from the F center site, are larger than those for the face diagonal F(110) ion. In other words, the unpaired spin density of the F center electron turns out to be larger on more distant ions than on closer ones. [Due to the T_d symmetry of the defect, four F(11 $\bar{1}$) ions are not equivalent to four F(111) ions and have much smaller hf couplings. Here and below, $\bar{1}$ stands for -1 .]

In the early work by Stoneham *et al.*,⁴² the point ion method has been used to obtain a wave function of the localized defect electron. For the s -type spherically symmetric wave function, the calculated hf couplings were in a very poor agreement with the experimental data, being overestimated by a factor of ~ 1.4 for F(100) and F(110) and underestimated by a factor of ~ 10 for F(11 $\bar{1}$) ions. The above-mentioned peculiarity has not been reproduced. Admixture of an f -type component to the wave function slightly cured the situation for the anisotropic part of the hf tensor of F(11 $\bar{1}$) and F(111) ions, while the isotropic part was still underestimated by the factor of 6 or 7 depending on the ion site. It was concluded that the resulting wave function was overlocalized due to the lack of the exchange and correlation interactions of the defect electron with the rest of the crystal. Another conclusion of this work was that the contribution of the f_{xyz} function is essential for a correct description of the F center charge density distribution. Since that time, several theoretical works on the properties of F centers in CaF₂ (Refs. 32–36) and BaF₂ (Refs. 66 and 67) have appeared. However, none of these reports contain theoretically calculated hf coupling constants.

Here, we investigate the dependence of the F center hf constants on the basis set and the size of the quantum cluster. The results of these calculations are summarized in Table II. The data shown in column 1 have been obtained using the small QM cluster Ca₄F₇, which contains only the first shell of the fluorine neighbors of the F center. This cluster has been

used to design basis set BASIS1, as described in Sec. II C. Since this QM cluster is small and, therefore, it can provide information about the values of the hf constants for the nearest neighbors of the F center only.

The hf constants calculated using the same basis BASIS1 and QM cluster $\text{Ca}_{16}\text{F}_{33}$ (column 2) are in qualitative and satisfactory quantitative agreement with the experimental data. In this case, not only the hf coupling constants calculated for F(111) ions are larger than those obtained for F(110) ions, as they should be, but also there is a good overall agreement between the calculated and measured hf constants for five shells of the fluorine ions near the F center. The corresponding spin density is shown in Fig. 2. Mulliken population analysis of the spin density suggests that approximately 65% of the electron spin is associated with the vacancy site and 6% with each of the nearest Ca ions. The spin charge associated with other atoms does not exceed 1%. A similar picture of the spin density distribution arises from the Natural Population Analysis (NPA).⁶⁸ In this case, $\sim 30\%$ of the electron spin is associated with the vacancy site, while 15% is assigned to each of the four Ca near it. Thus, according to NPA, $\sim 10\%$ of the spin density is beyond the vacancy and its nearest neighbors, which is consistent with the experimental observation of the F center hyperfine interaction with F atoms in as far as the seventh neighboring shell.

For comparison, we provide the results obtained using the same $\text{Ca}_{16}\text{F}_{33}$ QM cluster and standard basis sets: D95 basis on anions and LANL2DZ basis and ECP on cations (column 3). It is clear that the spin density distribution, as indicated by the values of the hf constants, is reproduced incorrectly in this case. We note that the Ca LANL2DZ basis does not contain d functions, while Ca atoms near the F center have two such basis functions in the case of BASIS1. Hence, we conclude that the presence of polarization functions is necessary for accurate modeling of the F center spin density distribution.

The lattice distortion induced by the F center is quite small. In the fully relaxed configuration, four nearest cations displace outward with respect to their lattice sites by 0.043 \AA , i.e., by 1.6% of the F-F separation. The six nearest anions move toward the F center by 0.023 \AA , and four F(111) fluorines move away from it by 0.028 \AA .

The F center ground state is formed by a $1s$ orbital perturbed by a crystalline field of T_d symmetry and contains an admixture of an f_{xyz} function as well as contributions due to atomic orbitals of the neighboring ions. A one-electron energy level of this state is situated in the band gap at 8.4 eV above the top of the valence band (VB). The lowest virtual orbital is the F center $2s$ function; it is situated at 13.3 eV above the top of the VB. Three degenerate $2p$ orbitals follow next at $\sim 13.44 \text{ eV}$. The one-electron band gap obtained for the same cluster is 12.4 eV , i.e., both $2s$ and $2p$ orbitals of the F center are situated above the bottom of the conduction band (CB). This may suggest that the corresponding states are either quasilocal or situated in the band gap near the bottom of the CB and can be thermally ionized even at relatively low temperatures. The band gap calculated using the ΔSCF method as the lowest singlet-triplet transition is only 11.0 eV due to the electrostatic interaction of the electron and the hole confined to the QM cluster. However, this does not affect the physical picture presented above.

Optical absorption energies of the F center have been calculated using the TDDFT technique. The three lowest excited states are degenerate and correspond to $1s \rightarrow 2p$ transitions of the F center with an excitation energy of 3.23 eV and oscillator strength $f = 0.133$ each. This energy value is in excellent agreement with the experimental position of the OA band maximum at 3.3 eV . We note that quantum-chemical techniques such as, for example, the coupled-cluster method with single and double excitations (CCSD) and its higher-order alternatives, can provide a more accurate description of the excited states.^{70,71} However, these methods are computationally demanding and require very high-quality basis sets, which makes it difficult to use them for extended systems. For example, the lowest F center excitation energy calculated using the Ca_4F_7 cluster, the CCSD method, and BASIS1 is 4.6 eV . As the quality of the basis set is increased, this excitation energy decreases to 4.1 eV , when a more advanced and significantly more computationally demanding basis cc-pVTZ is used. However, even with this basis set, the excitation energy is not converged.

The forbidden $1s \rightarrow 2s$ transition has the calculated energy of 3.48 eV . Higher-energy transitions with nonzero oscillator strengths are three degenerate transitions with excitation energies of 4.27 eV and oscillator strengths of 0.012 for each transition. They can be interpreted as intradefect $1s \rightarrow 3p$ transitions. We have also performed a ΔSCF calculation of the lowest excited state of the F center, i.e., the $2p$ state, making use of the fact that ground and excited states have different symmetries. The ΔSCF energy of the $1s \rightarrow 2p$ transition is 3.12 eV , which is in good agreement with the excitation energies both observed experimentally and calculated using TDDFT.

To reveal the effect of the cluster size on the excitation energies, we calculated the $1s \rightarrow 2p$ transition energy using a small QM cluster Ca_4F_7 and the same B3LYP-40 functional and BASIS1 basis set. The obtained excitation energy is 5.35 eV , i.e., it is overestimated by $\sim 2 \text{ eV}$ with respect to both the experimental optical absorption band and the one calculated using QM cluster $\text{Ca}_{16}\text{F}_{33}$. To rationalize this difference, we note that both $1s$ and $2p$ one-electron states of the F center are confined within the QM cluster borders. The effect of this confinement is the strongest for the $2p$ states in the small QM cluster, which result in an overestimated kinetic energy contribution to their one-electron energies and, consequently, overestimated corresponding transition energies.

The results of this section lead us to conclude that the functional B3LYP-40, together with the BASIS1 basis set, provide an accurate description of the energies and spatial distribution of the F center electronic states in the CaF_2 crystal. This is manifested by the values of the hyperfine constants (see Table II) and optical absorption energies calculated for this defect. Both sets of data demonstrate that first, second, and third neighboring shells of the defect site need to be included in the QM cluster.

B. Substitutional O^- ion

Isolated substitutional O^- impurities form during photodissociation of $\text{O}^{2-}-V_A$ dipoles.^{23,30} These defect centers

TABLE III. Calculated and experimental values of the hyperfine coupling constants (in Gauss) for the substitutional O⁻ ion.

Ion	Ca ₁₆ F ₃₃		Ca ₄ F ₇		Expt. (Ref. 69)	
	A	Axis	A	Axis	A	Axis
O(000)	-116.43	$\langle 001 \rangle$	-114.03	$\langle 001 \rangle$	97.8	$\langle 001 \rangle$
	7.68	\perp	10.00	\perp	9 \pm 6	\perp
F(001)	63.79	$\langle 001 \rangle$	57.12	$\langle 001 \rangle$	63.6	$\langle 001 \rangle$
	20.69	$\langle 110 \rangle$	16.60	$\langle 110 \rangle$	15.4 \pm 0.5	\perp
	20.39	$\langle \bar{1}\bar{1}0 \rangle$	16.46	$\langle \bar{1}\bar{1}0 \rangle$	15.4 \pm 0.5	\perp
F(100)	-3.98	$\langle 100 \rangle$	-3.59	(0.0, 0.99, 0.15)	3.6 \pm 0.5	$\langle 100 \rangle$
	-2.24	(0.0, 0.87, -0.49)	-2.72	(0.0, -0.15, 0.99)	3.4 \pm 0.5	$\langle 001 \rangle$
	-2.04	(0.0, 0.49, 0.87)	-1.57	$\langle 100 \rangle$	1.2 \pm 0.8	$\langle 010 \rangle$

were studied experimentally by means of EPR spectroscopy.⁶⁹ No optical absorption associated with the O⁻ ions has been observed.

We have calculated this defect using Ca₄F₇ and Ca₁₆F₃₃ embedded QM clusters. The O⁻ ion is a classical example of the Jahn-Teller defect, which induces asymmetric lattice relaxation and lowers the local symmetry from T_d to D_{2d} . The hole $2p$ orbital, i.e., the unoccupied $2p$ orbital, is directed along one of the $\langle 001 \rangle$ crystalline axes, which is further denoted as the z axis. The same axis is the fourth-order mirror-rotational axis of the D_{2d} symmetry group. Two nearest F(001) fluorines situated on the z axis displace toward the O⁻ ion by 0.1 Å, while four other nearest F(100) fluorines displace from it by 0.06 Å. The four nearest Ca ions displace by 0.05 Å. The direction of their displacement is toward the O⁻ ion along the z axis and away from it in the xy plane. The displacements of all other lattice ions do not exceed 0.04 Å.

The hyperfine parameters of the defect calculated in both clusters are shown in Table III together with the corresponding experimental values. Where convenient, the principal axes of the hf couplings tensor are shown in terms of the crystalline axes, while in other cases they are given in directional cosines. The calculated hf constants are in a reasonable agreement with the experimental data for both clusters. For example, the relative error for the largest component does not exceed 20%. This suggests that this defect has a small radius, at least in the ground state. Some of the calculated constants are negative, while the corresponding experimental constants⁶⁹ are reported without the sign.

The lowest optical transitions calculated with TDDFT in the Ca₁₆F₃₃ cluster are due to the electron transfer from the $2p_x$ and $2p_y$ orbitals of the oxygen impurity to its $2p_z$ orbital and correspond to the reorientation of the hole orbital. These transitions have an energy of 0.40 eV and zero oscillator strength. The next group of transitions is situated at about 7 eV and is related to the hole transfer from the O⁻ ion to the valence-band states. Only one transition has a considerable oscillator strength of 0.076 and an energy of 7.07 eV.

According to this result, substitutional O⁻ ions should induce an optical absorption band in the VUV region near 7 eV. However, such an absorption band has never been observed experimentally, most likely, due to the overlap with the bands of other oxygen-containing defects. One way to verify the

existence of the O⁻ absorption experimentally is correlating the intensities of the O⁻ EPR signal and the absorption bands in the VUV region.

C. O²⁻-V_A dipole

Properties of a complex formed by a substitutional oxide ion impurity and an anion vacancy, denoted as O²⁻-V_A dipole for brevity, have been intensively studied experimentally. For example, thermally induced reorientation and association of the dipoles has been investigated by the thermostimulated depolarization technique^{72,73} and their optical absorption and emission have been described in Refs. 23, 29, and 30. However, accurate theoretical modeling of the atomic-scale mechanisms in the O²⁻-V_A dipole is still lacking. Previously, we have described the mechanisms of the O²⁻-V_A dipole migration and reported the corresponding activation energies and discussed possible mechanisms of the photodissociation of these dipoles.³¹

In this section, we are concerned with the optical absorption and emission associated with the bulk O²⁻-V_A dipoles. Cluster Ca₁₄F₂₈ has been used for these calculations. The oxygen-vacancy dipole induces considerable lattice distortions, so the oxide ion displaces toward the vacancy site by 0.19 Å. Five fluorine ions nearest to the vacancy displace toward it by 0.25 Å, while four fluorines nearest to the oxygen ion in the xy plane displace away from it by 0.15 Å. All six calcium ions near the vacancy and the O²⁻ ion displace by 0.18 Å in a general direction from the vacancy to the oxide ion. In general, the equilibrium geometrical structure of the defect is very close to that reported in Ref. 31 in spite of the difference in the basis sets and the density functional.

In order to describe the optical transitions due to the dipoles, it is convenient to introduce a local coordinate system so the z axis is oriented parallel to the line connecting the oxygen ion and the anion vacancy site. Then, the three highest occupied one-electron states are dominated by $2p$ orbitals of the oxygen ion ($2p_x + 2p_y$, $2p_z$, and $2p_x - 2p_y$) with one-electron energies of 3.50, 3.51 and 3.62 eV above the top of the VB, respectively. These occupied orbitals are denoted as $p_{x+y}(\text{O})$, $p_z(\text{O})$, and $p_{x-y}(\text{O})$ and their spatial distribution is shown in Fig. 3. It should be noted that $p_{x+y}(\text{O})$ and $p_{x-y}(\text{O})$ have similar structures but they are not degenerate because the symmetry group of the defect is C_{2v} and it has only one-dimensional irreducible representations. The lowest

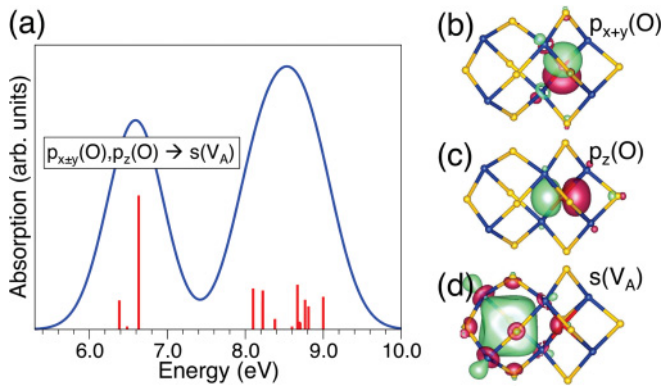


FIG. 3. (Color online) Calculated optical absorption spectrum of the $O^{2-}-V_A$ dipole (a) and one-electron states participating in the most intense optical absorption transition (b)–(d).

unoccupied orbital (LUMO) can be identified with the $1s$ wave function of the vacancy and is denoted as $s(V_A)$ (see Fig. 3). The corresponding one-electron energy level is 11.90 eV above the top of the VB. Two higher-energy unoccupied states, denoted as v_2 and v_3 , have complex characters and are formed by comparable contributions of atomic orbitals of several atoms.

The optical absorption spectrum calculated with TDDFT is shown in Fig. 3. The lowest absorption band is formed by the transitions from the $2p$ states of the oxygen ion to the $1s$ state of the vacancy, i.e., $p_{x+y}(O) \rightarrow s(V_A)$, $p_{x-y}(O) \rightarrow s(V_A)$, and $p_z(O) \rightarrow s(V_A)$. These transitions have excitation energies of 6.38, 6.48, and 6.63 eV, respectively, with the latter being the most intensive. The shape and position of this band agree very well with the experimental absorption band at 6.7 eV.³⁰

The second calculated OA band is centered at ~ 8.5 eV, which is also in excellent agreement with the experimentally observed band at 8.4 eV.³⁰ The low-energy part of this band consists of the transitions from the same $p_{x\pm y}(O)$, $p_z(O)$ states of the oxygen ion into $v_{2,3}$ orbitals having the energies in the range 8.1–8.6 eV. The transitions forming the higher-energy part yet are of more complicated nature and their one-electron interpretation is difficult.

The smooth curve shown in Fig. 3 is a convolution of Gaussian-type functions, each centered at the excitation energy of the corresponding transition and weighed with the value of the corresponding oscillator strength. The full width at half maximum (FWHM) for all Gaussians is 0.4 eV.

Figure 4 shows schematically the potential energy surfaces of the ground state (E_0) and three lowest excited states. In the case of the $O^{2-}-V_A$ dipole, these excited states correspond to the $p_{x\pm y}(O) \rightarrow s(V_A)$ ($E_{1,2}$) and $p_z(O) \rightarrow s(V_A)$ (E_3) charge-transfer transitions from $2p$ orbitals of the oxygen ion into the vacancy $1s$ orbital. These transitions are indicated with the arrows originating at the ground state's energy minimum.

Calculating the luminescence energies requires finding the minimum of the potential energy surface for the corresponding excited states. Unfortunately, doing this using TDDFT is extremely computationally expensive. Therefore, we determined the potential energy minimum for the lowest-energy triplet excited state, shown in Fig. 4 with a white circle, using the Δ SCF method.

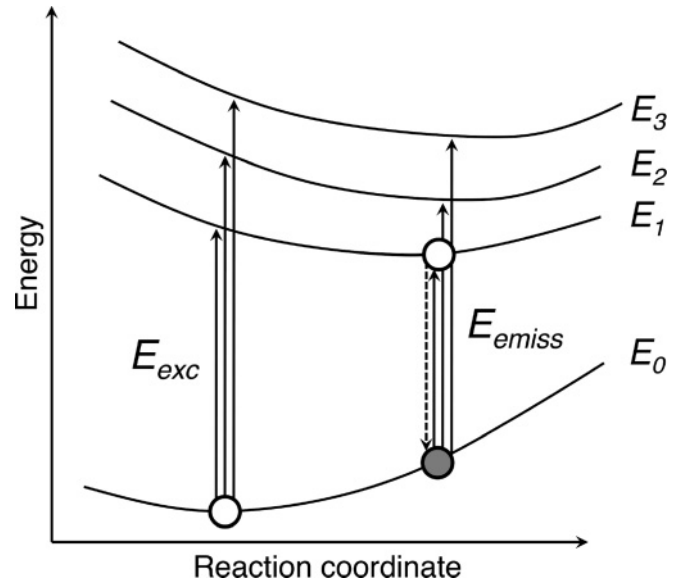


FIG. 4. Schematics of potential energy surface for the ground state (E_0) and three lowest-energy excited states ($E_{1,2,3}$) of the $O^{2-}-V_A$ defect. The energy minima are shown with white circles. The vertical lines indicate singlet-singlet excitation energies calculated using TDDFT. The dashed line shows the triplet-singlet energy splitting calculated using the Δ SCF method. See text for details.

This lowest triplet excited state corresponds to the $p_{x+y}(O) \rightarrow s(V_A)$ transition. The local lattice distortion in this fully relaxed excited state is much smaller than that in the ground state. This is an expected result since both defect components in this case (they are O^- ion and the adjacent F center) are neutral with respect to the crystal lattice, in contrast to the ground state. The displacements of ions from their ideal lattice sites do not exceed 0.1 Å.

The luminescence energy calculated for this geometrical structure using Δ SCF corresponds to the triplet \rightarrow singlet transition (indicated with the dashed line in Fig. 4) and has the value of 1.71 eV, which is significantly smaller than the experimental value of 2.67 eV.³⁰ This luminescence energy can also be determined as an excitation energy from the ground state to an excited state, where the corresponding geometrical structure of the ground state is shown in Fig. 4 using the shaded circle.

We have calculated the energies for several singlet \rightarrow singlet transitions for this geometrical structure using the TDDFT method. Here, we assume that these singlet excited states have their energy minima at approximately the same geometrical configuration as the lowest triplet excited state. We found that the three lowest excited states correspond to the transitions from $p_{x\pm y}(O)$ and $p_z(O)$ states into $s(V_A)$ with respective luminescence energies of 1.99, 2.23, and 3.00 eV. The oscillator strengths of the first two transitions are ~ 0.001 , while for the third one it is 0.116.

Taking into account that the latter transition is dominant and that the calculated emission energy is in a reasonable agreement with the experimentally observed value (2.6 eV), we suggest that the $s(V_A) \rightarrow p_z(O)$ transition is the most efficient luminescence channel for the $O^{2-}-V_A$ defect. It can also be concluded that nonradiative transitions from E_3 to

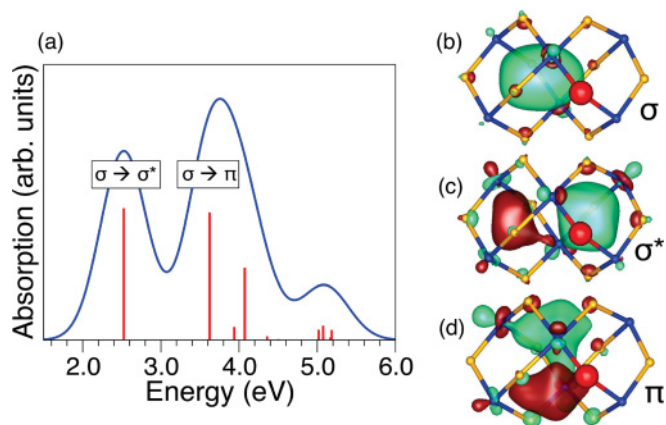


FIG. 6. (Color online) The calculated optical absorption spectrum (a) and the lowest-energy one-electron states for an $F_{2A}^+(O^{2-})$ center: (b) σ bonding orbital, (c) σ^* antibonding orbital, and (d) π -like orbital.

their displacements range from 0.15 to 0.30 Å. The oxygen ion moves toward the nearest vacancy by 0.12 Å. Despite the unequal electron occupation of the vacancies, this defect can be seen as an F_2^+ center, rather than an $F-V_A$ complex, perturbed by the O^{2-} ion.

The character of the charge density distribution in the $F_{2A}^+(O^{2-})$ center is reflected in the values of the corresponding hyperfine interaction parameters (Fig. 5). We report only two values of hf coupling for each ion. This is because the hf tensors for all ions are nearly axial; the deviation from the axial symmetry, defined as the ratio $\frac{|A_2 - A_3|}{A_1}$, does not exceed 2%. This allows us to provide one value of A_{\parallel} with corresponding principal axis (shown with arrows in the figure), while for both perpendicular directions, the hf values are the same and are given as A_{\perp} . The fluorine ions near the vacancy A have larger hf coupling values than those near vacancy B, which is a reflection of the uneven spin density distribution.

The calculated optical absorption spectrum is shown in Fig. 6. The spectrum has three distinct bands. The lowest one is centered at 2.52 eV and is assigned to the electron transition from a σ bonding to a σ^* antibonding orbital of the perturbed F_2^+ center. These orbitals are shown in Figs. 6(b) and 6(c), respectively. The second band is formed by three transitions with energies 3.62, 3.94, and 4.07 eV, of which the first and the third transitions are more intensive ones. The excited states, corresponding to these transitions, have the nature of perturbed π -like orbitals of the $F_{2A}^+(O^{2-})$ center, i.e., they are formed by p orbitals of the vacancy states oriented perpendicularly to the line connecting the vacancies. One of these states is shown in Fig. 6(d). Finally, the third band has its maximum at about 5 eV and is composed of several transitions. The orbitals of the corresponding excited states have complex structures and are not shown in the figure.

It is known from the experimental data²³ that the $F_{2A}^+(O^{2-})$ center has two optical absorption bands at 2.3–2.4 and at 3.4 eV, which have approximately equal intensities. Thus, the calculated optical absorption bands are in a good agreement with these data (within 0.2 eV).

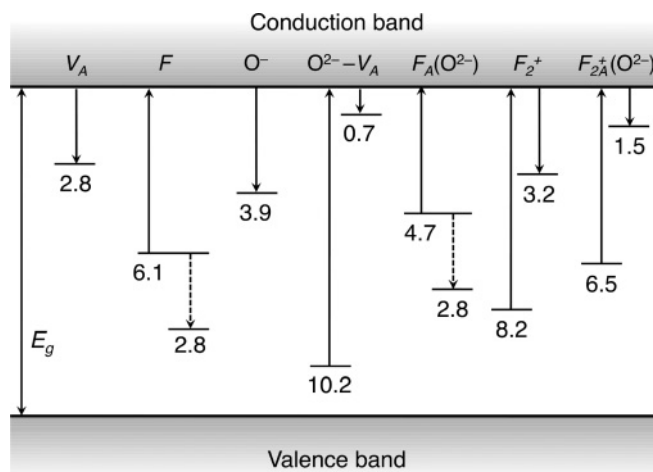


FIG. 7. Calculated energy levels of the defects. Solid up and down arrows indicate vertical ionization potentials and vertical affinities, respectively. Dashed down arrows indicate the energy gain due to the defect relaxation immediately after ionization. E_g shows the one-electron band gap. All values are given in eV.

F. Charge trapping at the point defects

In order to investigate the ability of defects to be ionized by UV light and, conversely, to trap electrons moving at the bottom of the CaF_2 conduction band, we calculated “vertical” ionization potentials (IP) and electron affinities for several defects. The vertical ionization potentials are calculated as

$$\text{IP} = E(D - e^-) + E(\text{CaF}_2 + e^-) - [E(D) + E(\text{CaF}_2)],$$

where $E(D)$ is the total energy of the defect in its lowest-energy geometrical configuration and $E(D - e^-)$ is the total energy of the ionized defect in the same configuration, $E(\text{CaF}_2)$ is the energy of the nondefective CaF_2 QM cluster and $E(\text{CaF}_2 + e^-)$ is the energy of the same cluster with one electron at the bottom of the conduction band. Similarly, the vertical electron affinities of defects are calculated as

$$\text{EA} = E(D) + E(\text{CaF}_2 + e^-) - [E(D + e^-) + E(\text{CaF}_2)],$$

where $E(D + e^-)$ is the total energy of the negatively charged defect calculated in the geometrical structure corresponding to its neutral state. In addition, in some cases, we considered the energy due to the defect relaxation after ionization. Since the positions of the energy levels are determined using the IP and EA calculated with respect to the conduction band, it is natural to plot these levels with respect to the conduction-band edge (see Fig. 7). For completeness, we also plot the valence-band edge schematically. Since neither the top of the valence band nor the band gap enter these calculations, the exact value of the band gap E_g in Fig. 7 is irrelevant.

The results of these calculations are summarized in Fig. 7. Clearly, neutral [F , $O^{2-}-V_A$, and $F_2^+(O^{2-})$], negatively charged [$F_A(O^{2-})$], and positively charged (F_2^+) defects have levels within the band gap and can be ionized by sub-band-gap UV light. Importantly, while the IPs of the F and F_2^+ centers due to anion vacancies alone are 6.1 and 8.2 eV, the IPs of similar defects in the vicinity of substitutional O^{2-} ions reduce to 4.7 and 6.5 eV, respectively.

On the other hand, positively charged defects V_A , O^- , and F_2^+ have vertical electron affinities of $\sim 3\text{--}4$ eV and can readily trap electrons from the bottom of the conduction band. Moreover, even neutral defects $O^{2-}-V_A$ and $F_2^+(O^{2-})$ have non-negligible vertical electron affinity and can also trap electrons. Thus, the presence of oxygen-containing defects creates additional channels for the photoinduced defect transformation.

We notice that once the charge state of a defect changes, the atoms in its vicinity displace so as to adopt positions corresponding to the energy minimum on the new potential energy surface. The energy released in this process is called relaxation energy. It is released in the form of lattice vibrations and its amount depends on the particular defect structure. In Fig. 7, we show that relaxation energy corresponding to the transformation of a neutral F center to a positively charged anion vacancy V_A is ~ 2.8 eV. A similar value has been obtained for the transformation of a negatively charged $F_A(O^{2-})$ center to a neutral $O^{2-}-V_A$ center. This suggests that not only the electronic structure of the F center component of an $F_A(O^{2-})$ center is similar to that of an isolated F center, but also the atomic displacements due to the F center ionization are similar in the two systems. Thus, the field of the atomic displacements near an $O^{2-}-V_A$ center can be well approximated by a superposition of the atomic displacements due to a positively charged anion vacancy and a negatively charged substitutional O^{2-} ion.

IV. SUMMARY AND CONCLUSIONS

Our results provide a comprehensive characterization of several defects formed by anion vacancies and oxygen impurities in the bulk CaF_2 . Using an embedded cluster method and *ab initio* calculations, we accurately reproduce the existing spectroscopic data on relatively simple defects and predict the properties of more complex defects, combining several vacancy and impurity centers.

The versatile computational approach used in this work allows one to judiciously select an appropriate size and shape of the QM region, apply HF, hybrid DFT and “beyond”-DFT *ab initio* methods, and calculate a wide range of spectroscopic properties.

The computational method, density functional, and the basis set have been tested for the F center and $O^{2-}-V_A$ defects. The calculated properties are generally in good agreement with available experimental data. For example, the discrepancies between the experimental and calculated electronic paramagnetic resonance parameters do not exceed

15%. In particular, in the case of the bulk F center, we successfully reproduced a highly anisotropic distribution of the spin density up to the fifth shell of the lattice anions. The optical absorption energies, calculated using the TDDFT technique, differ from the corresponding experimental values by no more than 0.2–0.3 eV. This gives our calculation predictive strength for calculating properties of complex defect structures.

We predict that the substitutional O^- ion has the OA band at about 7 eV. An experimental observation of this absorption band is complicated by the presence of other oxygen centers having optical absorption in the same energy region. We suggest that this difficulty might be overcome if the intensity of the optical absorption is correlated with the intensity of the corresponding O^- EPR signature.

We determined the one-electron states involved in the optical absorption and emission in the $O^{2-}-V_A$ defect and found that the maximum of the 6.7-eV absorption band is associated with the third lowest-energy transition $p_z(O) \rightarrow s(V_A)$. The luminescence band is associated with the corresponding $s(V_A) \rightarrow p_z(O)$ transition with a calculated energy of 3.0 eV. We suggest that the first and second lowest excited states do not contribute to the emission because of negligible values of the corresponding transition intensities. Similarly, for the $F_{2A}^+(O^{2-})$ center, in which the two vacancies are closest to each other, the calculated optical absorption spectrum agrees well with the experimental data.

Finally, we demonstrated that substitutional oxygen species create additional channels for the photoinduced defect transformation and give rise to both deep and shallow electron traps. The extent of the lattice relaxation around such defects strongly depends on their structure and the charge state. Both of these issues create significant problems in using CaF_2 for nanolithography applications. However, the richness of such defect-induced optical absorption and emission features might be used in other applications such as photodetection and sensory functions, which can be further advanced by exploiting a recently demonstrated property of birefringent materials to form invisibility cloak for macroscopic objects.⁷⁵

ACKNOWLEDGMENTS

The authors gratefully appreciate the use of the UCL Research Computing facility and membership of the UK’s HPC Materials Chemistry Consortium, which is funded by EPSRC (EP/F067496). A.S.M. is grateful to University College London and Universität Osnabrück for the hospitality and funding during his visits. P.V.S. is supported by the Royal Society.

*andrem@igc.irk.ru

¹T. K. Allison, J. van Tilborg, T. W. Wright, M. P. Hertlein, R. W. Falcone, and A. Belkacem, *Opt. Express* **17**, 8941 (2009).

²R. Huber, H. Satzger, W. Zinth, and J. Wachtveitl, *Opt. Commun.* **194**, 443 (2001).

³C. Nagura, A. Suda, H. Kawano, M. Obara, and K. Midorikawa, *Appl. Opt.* **41**, 3735 (2002).

⁴I. Buchvarov, A. Trifonov, and T. Fiebig, *Opt. Lett.* **32**, 1539 (2007).

⁵U. Megerle, I. Pugliesi, C. Schrieffer, C. F. Sailer, and E. Riedle, *Appl. Phys. B: Lasers Opt.* **96**, 215 (2009).

⁶G. W. Rubloff, *Phys. Rev. B* **5**, 662 (1972).

⁷M. Rothschild, *Mater. Today* **8**, 18 (2005).

⁸T. Westerhoff, K. Knapp, and E. Moersen, in *Proceedings of the Society of Photo-Optical Instrumentation Engineers*, edited by A. J. Marker (SPIE, Bellingham, WA, 1998), Vol. 3424, pp. 10–19.

⁹C. A. Klein, *J. Appl. Phys.* **100**, 083101 (2006).

¹⁰J. M. Ko, S. Tozawa, A. Yoshikawa, K. Inaba, T. Shishido, T. Oba, Y. Oyama, and T. Kuwabara, *J. Cryst. Growth* **222**, 243 (2001).

¹¹J. Y. Xu, M. L. Shi, B. L. Lu, X. H. Li, and A. H. Wu, *J. Cryst. Growth* **292**, 391 (2006).

- ¹²J. T. Mouchovski, K. A. Temelkov, N. K. Vuchkov, and N. V. Sabotinov, *J. Phys. D: Appl. Phys.* **40**, 7682 (2007).
- ¹³J. H. Burnett, Z. H. Levine, and E. L. Shirley, *Phys. Rev. B* **64**, 241102 (2001).
- ¹⁴M. Letz, L. Parthier, A. Gottwald, and M. Richter, *Phys. Rev. B* **67**, 233101 (2003).
- ¹⁵B. L. Wang, R. R. Rockwell, and J. List, *J. Microlith. Microfab.* **3**, 115 (2004).
- ¹⁶M. Letz, A. Engel, W. Mannstadt, L. Parthier, U. Natura, and K. Knapp, in *Optical Microlithography XVII*, edited by B. W. Smith (SPIE, Bellingham, WA, 2004), Vol. 5377, pp. 1797–1804.
- ¹⁷J. Sils, S. Hausfeld, W. Clauss, U. Pahl, R. Lindner, and M. Reichling, *J. Appl. Phys.* **106**, 063109 (2009).
- ¹⁸A. Molchanov, J. Friedrich, G. Wehrhan, and G. Müller, *J. Cryst. Growth* **273**, 629 (2005).
- ¹⁹J. T. Mouchovski, *Prog. Cryst. Growth Charact. Mater.* **53**, 79 (2007).
- ²⁰C. Görling, U. Leinhos, and K. Mann, *Opt. Commun.* **249**, 319 (2005).
- ²¹S. Gogoll, E. Stenzel, H. Johansen, M. Reichling, and E. Matthias, *Nucl. Instrum. Methods Phys. Res., Sect. B* **116**, 279 (1996).
- ²²S. Gogoll, E. Stenzel, M. Reichling, H. Johansen, and E. Matthias, *Appl. Surf. Sci.* **96–98**, 332 (1996).
- ²³E. Radzhabov and P. Figura, *Phys. Status Solidi B* **136**, K55 (1986).
- ²⁴E. Radzhabov, *Phys. Status Solidi B* **180**, 513 (1993).
- ²⁵E. Radzhabov, in *Proceeding of the 13th International Conference on Defects in Insulating Materials (ICDIM'96)*, edited by G. E. Matthews and R. T. Williams, Vol. 239, (1997), pp. 261–266.
- ²⁶J. Sils, E. Radzhabov, and M. Reichling, *J. Phys. Chem. Solids* **68**, 420 (2007).
- ²⁷*Crystals with the Fluorite Structure: Electronic, Vibrational, and Defect Properties*, edited by W. Hayes (Clarendon, Oxford, 1974).
- ²⁸G. Gummer, *Z. Phys.* **215**, 256 (1968).
- ²⁹V. A. Arkhangel'skaya, V. M. Reiterov, and L. M. Trofimova, *Zh. Prikl. Spektrosk.* **32**, 103 (1980).
- ³⁰E. Radzhabov, *Phys. Status Solidi B* **136**, K139 (1986).
- ³¹A. S. Mysovsky, E. A. Radzhabov, M. Reichling, A. L. Shluger, and P. V. Sushko, *Phys. Status Solidi C* **2**, 392 (2005).
- ³²A. V. Puchina, V. E. Puchin, E. A. Kotomin, and M. Reichling, *Solid State Commun.* **106**, 285 (1998).
- ³³H. Shi, R. I. Eglitis, and G. Borstel, *Phys. Rev. B* **72**, 045109 (2005).
- ³⁴A. C. Lewandowski and T. M. Wilson, *Phys. Rev. B* **52**, 100 (1995).
- ³⁵M. Letz and L. Parthier, *Phys. Rev. B* **74**, 064116 (2006).
- ³⁶Y. Ma and M. Rohlfing, *Phys. Rev. B* **77**, 115118 (2008).
- ³⁷A. S. Foster, T. Trevethan, and A. L. Shluger, *Phys. Rev. B* **80**, 115421 (2009).
- ³⁸A. M. Burow, M. Sierka, J. Döbler, and J. Sauer, *J. Chem. Phys.* **130**, 174710 (2009).
- ³⁹H. Shi, R. I. Eglitis, and G. Borstel, *Comput. Mater. Sci.* **39**, 430 (2007).
- ⁴⁰S. M. Botis, D. A. Adriaens, and Y. M. Pan, *Phys. Chem. Miner.* **36**, 1 (2009).
- ⁴¹W. Hayes and J. P. Stott, *Proc. R. Soc. London, Ser. A* **301**, 313 (1967).
- ⁴²A. M. Stoneham, W. Hayes, P. H. S. Smith, and J. P. Stott, *Proc. R. Soc. London, Ser. A* **306**, 369 (1968).
- ⁴³B. C. Cavenett, W. Hayes, I. C. Hunter, and A. M. Stoneham, *Proc. R. Soc. London, Ser. A* **309**, 53 (1969).
- ⁴⁴B. G. Dick and A. W. Overhauser, *Phys. Rev.* **112**, 90 (1958).
- ⁴⁵M. J. Frisch, G. W. Trucks, H. B. Schlegel, G. E. Scuseria, M. A. Robb, J. R. Cheeseman, V. G. Zakrzewski, J. A. Montgomery Jr., R. E. Stratmann, J. C. Burant *et al.* (unpublished).
- ⁴⁶P. V. Sushko, A. L. Shluger, and C. R. A. Catlow, *Surf. Sci.* **450**, 153 (2000).
- ⁴⁷V. B. Sulimov, P. V. Sushko, A. H. Edwards, A. L. Shluger, and A. M. Stoneham, *Phys. Rev. B* **66**, 024108 (2002).
- ⁴⁸D. Muñoz Ramo, P. V. Sushko, J. L. Gavartin, and A. L. Shluger, *Phys. Rev. B* **78**, 235432 (2008).
- ⁴⁹A. V. Kimmel, D. Muñoz Ramo, P. V. Sushko, A. L. Shluger, and M. M. Kuklja, *Phys. Rev. B* **80**, 134108 (2009).
- ⁵⁰J. S. Braithwaite, P. V. Sushko, K. Wright, and C. R. A. Catlow, *J. Chem. Phys.* **116**, 2628 (2002).
- ⁵¹M. L. Sushko, P. V. Sushko, I. V. Abarenkov, and A. L. Shluger, *J. Comput. Chem.* **31**, 2955 (2010).
- ⁵²P. V. Sushko and I. V. Abarenkov, *J. Chem. Theory Comput.* **6**, 1323 (2010).
- ⁵³I. V. Abarenkov, *Phys. Rev. B* **76**, 165127 (2007).
- ⁵⁴N. W. Winter, R. M. Pitzer, and D. K. Temple, *J. Chem. Phys.* **86**, 3549 (1987).
- ⁵⁵W. R. Wadt and P. J. Hay, *J. Chem. Phys.* **82**, 284 (1985).
- ⁵⁶D. R. Huffman and M. H. Norwood, *Phys. Rev.* **117**, 709 (1960).
- ⁵⁷*Handbook of Interatomic Potentials: I. Non Metals*, edited by A. M. Stoneham (AERE Harwell, Didcot, 1981).
- ⁵⁸G. Pacchioni, F. Frigoli, D. Ricci, and J. A. Weil, *Phys. Rev. B* **63**, 054102 (2000).
- ⁵⁹J. L. Gavartin, P. V. Sushko, and A. L. Shluger, *Phys. Rev. B* **67**, 035108 (2003).
- ⁶⁰A. L. Shluger, A. S. Foster, J. L. Gavartin, and P. V. Sushko, in *Nano and Giga Challenges in Microelectronics*, edited by J. Greer, A. Korkin, and J. Labanowski (Elsevier, Amsterdam, 2003), pp. 151–222.
- ⁶¹A. S. Mysovsky, E. A. Radzhabov, M. Reichling, A. L. Shluger, and P. V. Sushko, *Izv. VUZOV, Stroit. Arkhit.* **4**, 101 (2006).
- ⁶²A. D. Becke, *J. Chem. Phys.* **98**, 1372 (1993).
- ⁶³C. Lee, W. Yang, and R. G. Parr, *Phys. Rev. B* **37**, 785 (1988).
- ⁶⁴A. V. Kimmel, P. V. Sushko, and A. L. Shluger, *J. Non-Cryst. Solids* **353**, 599 (2007).
- ⁶⁵R. E. Stratmann, G. E. Scuseria, and M. J. Frisch, *J. Chem. Phys.* **109**, 8218 (1998).
- ⁶⁶J. M. Vail, W. A. Coish, H. He, and A. Yang, *Phys. Rev. B* **66**, 014109 (2002).
- ⁶⁷J. Chen, L. B. Lin, and F. Q. Jing, *Nucl. Instrum. Methods Phys. Res., Sect. B* **187**, 354 (2002).
- ⁶⁸A. E. Reed, R. B. Weinstock, and F. Weinhold, *J. Chem. Phys.* **83**, 735 (1985).
- ⁶⁹H. Bill and R. H. Silsbee, *Phys. Rev. B* **10**, 2697 (1974).
- ⁷⁰T. Kus, V. F. Lotrich, and R. J. Bartlett, *J. Chem. Phys.* **130**, 124122 (2009).
- ⁷¹K. Kowalski, S. Krishnamoorthy, O. Villa, J. R. Hammond, and N. Govind, *J. Chem. Phys.* **132**, 154103 (2010).
- ⁷²P. W. M. Jacobs and S. H. Ong, *J. Phys. Chem. Solids* **41**, 437 (1980).
- ⁷³W. Bollmann, *Cryst. Latt. Def. Amorph.* **7**, 139 (1977).
- ⁷⁴R. Rauch and G. Schwotzer, *Phys. Status Solidi A* **74**, 123 (1982).
- ⁷⁵X. Chen, Y. Luo, J. Zhang, K. Jiang, J. B. Pendry, and S. Zhang, *Nat. Commun.* **2**, 176 (2011).